From generalized stacking fault energies to dislocation properties: Five-energy-point approach and solid solution effects in magnesium

Zongrui Pei*
Max-Planck-Institut für Eisenforschung GmbH, D-40237 Düsseldorf, Germany
and Aachen Institute for Advanced Study in Computational Engineering Science (AICES), RWTH-Aachen University, D-52062 Aachen, Germany

Duancheng Ma
Max-Planck-Institut für Eisenforschung GmbH, D-40237 Düsseldorf, Germany

Martin Friák
Institute of Physics of Materials, Academy of Sciences of the Czech Republic, v.v.i., Žižkova 22, CZ-61662 Brno, Czech Republic; Max-Planck-Institut für Eisenforschung GmbH, D-40237 Düsseldorf, Germany; and Aachen Institute for Advanced Study in Computational Engineering Science (AICES), RWTH-Aachen University, D-52062 Aachen, Germany

Bob Svendsen
Aachen Institute for Advanced Study in Computational Engineering Science (AICES), RWTH-Aachen University, D-52062 Aachen, Germany and Max-Planck-Institut für Eisenforschung GmbH, D-40237 Düsseldorf, Germany

Dierk Raabe and Jörg Neugebauer
Max-Planck-Institut für Eisenforschung GmbH, D-40237 Düsseldorf, Germany

(Received 18 May 2015; revised manuscript received 25 July 2015; published 11 August 2015; corrected 29 October 2015)

Using *ab initio* calculations and symmetrized plane waves, we analyze the basal-plane generalized stacking fault energies in pure Mg and Mg-Y alloys and show that the knowledge of energies of only five specific points is sufficient to accurately predict the core structures and Peierls stresses of $\langle a \rangle$-type edge dislocations in these alloys. Our five-point approach substantially reduces the computational cost related to the Peierls-Nabarro (PN) model and allows for a high-throughput application of the PN model to study Peierls stress changes in Mg upon alloying. We employ our approach to study Mg binary alloys containing nine rare-earth (RE) and 11 other solutes. Based on the Peierls stresses of these 20 Mg alloys calculated from the Peierls-Nabarro model, the solutes are divided into three groups: (i) the first group, consisting of Be, Zn, Tl, Tc, Os, Ru, Re, and Co, when added as solutes into Mg, lead to more compact dislocation core structures and larger Peierls stresses than found for pure Mg. (ii) Elements in the second group, including Ti, Nd, Lu, Zr, Hf, La, and Pr change the core widths and Peierls stresses moderately. (iii) The solutes in the third group containing Y, Er, Tm, Ho, and Sc extend the stacking fault width, and the resulting Peierls stresses are generally very low. Based on an error analysis, we conclude that the first group has a clear solute strengthening effect and the third group has a clear solute softening effect, while the effects of the elements in the second group are too small to be resolved by the present approach.

DOI: 10.1103/PhysRevB.92.064107 PACS number(s): 31.15.A−, 61.72.Ff, 61.72.Hh, 61.72.Lk

I. INTRODUCTION

Magnesium and magnesium alloys are promising structural materials because of their low specific weight and relatively high strength [1,2]. Their wider commercial use, specifically for sheet forming applications is, however, hindered by their low ductility at room temperature. In order to improve the ductility of Mg alloys, it is necessary to analyze the underlying mechanisms controlling the brittle behavior. Dislocations are the most important extended defects closely related to the plastic mechanical properties of Mg alloys. Their core structure determines their mobility and further influences the yield stress and ductility through their influence on glide behavior, cross slip, and dislocation reactions to name but a few critical phenomena in that context. According to the von Mises criterion, homogeneous polycrystal deformation requires the activation of at least five independent slip or respective shear systems. Otherwise, the kinematic compatibility is violated and the material fails since an arbitrary externally imposed mechanical load cannot be accommodated by the material's internal degrees of shear [3,4]. For hcp Mg, the number of active deformation modes in one crystal is lower than five since shear is confined to basal slip.

As a complementary approach to performing corresponding systematic crystal mechanical experiments to gain insight into the deformation mechanisms, theoretical simulations of dislocation cores of both $\langle a \rangle$-type and $\langle c + a \rangle$-type dislocations have been performed [5–8]. Here, $\langle a \rangle$-type slip refers to dislocation shear inside the basal plane, while $\langle c + a \rangle$-type shear refers to slip involving out-of basal plane shear modes. To name a few examples, Yasi and co-workers [6] simulated the core structures of basal and prismatic dislocations by using the flexible boundary condition method and later the same

*z.pei@mpie.de

authors developed different models to calculate the critical resolved shear stresses (CRSS) of basal dislocations [9] and the cross-slip stresses of prismatic screw dislocations [10]. This knowledge was recently further combined with a solute strengthening effect by Leyson and co-workers in their simulations of basal dislocations of Mg-Al alloys [11]. As another example, Shin and Carter applied a previously developed orbital-free density functional theory (OFDFT) method and applied it to dislocation core structures [7] and, subsequently, also to Peierls stresses [8] in pure Mg.

The aforementioned atomistic-scale simulation methods belong to the direct methods or full-field approaches that address dislocation cores by explicitly constructing them in computer simulations in an atom-by-atom manner. The structure is subsequently relaxed by molecular dynamics simulations. The molecular dynamics simulations can be of quantum-mechanical nature as, e.g., the density functional theory based flexible boundary condition method (DFT-FBC) [12], or based on atomisitc interatomic potential simulations, such as embedded atom methods (EAM). It should be noted that the DFT-FBC simulations are accurate but computationally very expensive. Atomistic simulations are fast but there is lack of sufficiently reliable EAM potentials for Mg alloys that are sensitive enough to predict composition-dependent dislocation and plasticity trends.

Different from the direct methods, indirect methods do not describe the dislocation core structure explicitly but employ, e.g., the Peierls-Nabarro model [13]. The dislocation core structures can be analyzed by the two-dimensional Peierls-Nabarro model, which was developed by Leibfried and Dietze [14]. The primary input is taken from the generalized stacking fault energies (GSFEs, so-called gamma surface) proposed by Vitek [15]. The gamma surface can be accurately calculated by DFT methods. Therefore, Peierls-Nabarro modeling represents an alternative to the above discussed direct fully atomistic simulation methods for dislocations with simple core structures. In the last years, these models have been substantially improved and optimized. For example, Wang has added gradients of the misfit density to the total energy functional of dislocations in order to address dislocations possessing narrow cores [16]. The misfit density refers to the spatial variation of the dislocation's core misfit function as will be discussed in more detail below. Others have discretized the originally used arctan-type functions to describe the misfit density of dislocations in Al [17,18], since the discretized functions can provide more flexibility than the analytical (arctan-type) functions. The dislocation core structures in Mg are usually very complicated, but the basal dislocation has a dissociated planar core, which can be adequately described by a Peierls-Nabarro (PN) model. For example, very recently, Tsuru *et al.* employed a semidiscrete variational PN model to study the core structures and Peierls stresses of Mg and two Mg alloys, namely, Mg-Al and Mg-Y [19].

Despite numerous examples of applying the Peierls-Nabarro model to pure metals, its application to alloys is not straightforward. Calculations of gamma surfaces of alloys represent conceptional and computational challenges due to the vast configurational spaces of different atomic species. Here, we propose an efficient and at the same time accurate method, which is based on an approach that allows us to represent the full gamma surface using a few carefully selected sample points only. After carefully testing our proposed approach, we demonstrate its performance in a high-throughput study of an extensive set of Mg binary alloys containing 20 different types of solutes. For these, we accurately predict widely dissociated cores of basal-plane $\langle a \rangle$ dislocations and analyze the influence of solutes on the Peierls stress.

TABLE I. The elastic constants (all in GPa) of Mg taken from Ref. [21] that were used as input for the Peierls-Nabarro model, see Eq. (1).

Elatic constant	C_{11}	C_{12}	C_{13}	C_{33}	C_{44}	K_e	K_s
Value	59.5	26.1	21.8	61.6	16.4	1.96	1.31

II. METHODOLOGY

A. Peierls-Nabarro model

The equilibrium configuration of a dislocation is within the Peierls-Nabarro model determined by the balance of restoring force and elastic resistance of the crystal lattice. Let us suppose that we have an edge dislocation in a Cartesian coordinate. The dislocation line runs along the z axis (for screw dislocation the dislocation line runs along the x axis), slips in the xz plane and its Burgers vector $\vec{b}$ is parallel to x. The mathematical expression of such a dislocation is

$$2K \int_{-\infty}^{+\infty} \frac{\vec{\rho}(x')}{x - x'} dx' = -\frac{d\gamma(\vec{u})}{d\vec{u}}, \tag{1}$$

where the left side is the elastic resistance and the right side represents the restoring forces. Specifically, $\vec{u}$ is the misfit function and $\vec{\rho}(x)$ is the misfit density $\vec{\rho}(x) = d\vec{u}(x)/dx$. The generalized stacking fault energy, $\gamma(\vec{u})$, or gamma surface, is the key input quantity of the model. In the two-dimensional case, $\vec{u}$ is a vector consisting of components along x and z, u_x and u_z, respectively. Mathematically $\vec{u}$=(u_x, u_z). Further, K is a proportionality constant (so-called energy factor) that is in elastically isotropic materials described by the shear modulus μ and the Poisson ratio ν. $K = K_e = \mu/4\pi(1 - \nu)$ for edge dislocations and $K = K_s = \mu/4\pi$ for screw dislocations. The subscripts K_e and K_s indicate whether the constant is for an edge "e" or a screw "s" dislocation. In elastically anisotropic media, K depends on the slip system and dislocation character. For a basal $\langle a \rangle$ dislocation, $K_e = 1/4\pi(\bar{C}_{11} + C_{13})((C_{44}(\bar{C}_{11} - C_{13}))/(C_{33}(\bar{C}_{11} + C_{13} + 2C_{44})))^{1/2}$, $\bar{C}_{11} = (C_{11}C_{33})^{1/2}$; $K_s = 1/4\pi(C_{44}C_{66})^{1/2}$, $C_{66} = (C_{11} - C_{12})/2$ [20]. The values used in our simulations are summarized in Table I.

An analytical solution of $\vec{u}$ determined by Eq. (1) exists only for rather simple gamma surfaces. For more complex (and more realistic) gamma surfaces, solutions can be obtained only numerically. Often, the solution is obtained by expanding $\vec{u}$ into a series of arctan functions [13]. The arctan function is a suitable basis since it is the analytical solution to Eq. (1) when the gamma surface is expressed by one cosine function. Dislocations described by arctan-type functions are called Peierls dislocations.

Specifically, in our study, we focus on $\langle a \rangle$-type edge dislocations that are known to dissociate and where the

distance between the two partials is rather large [6]. This type of dislocations can be well described by only four arctan functions, i.e., two for the edge component and two for the screw component. The misfit functions are then written as follows:

$$u_x(x) = \frac{b}{2\pi}\arctan\frac{x-d_e/2}{w_e} + \frac{b}{2\pi}\arctan\frac{x+d_e/2}{w_e} + \frac{b}{2}, \tag{2a}$$

$$u_z(x) = \frac{\sqrt{3}b}{6\pi}\arctan\frac{x-d_s/2}{w_s} - \frac{\sqrt{3}b}{6\pi}\arctan\frac{x+d_s/2}{w_s}, \tag{2b}$$

where $u_x(x)$ and $u_z(x)$ describe the edge and the screw displacements, respectively. Here, d_e or d_s is the distance between the edge or screw components of the two partial dislocations and w_e or w_s is the width of the edge or screw components of the Peierls dislocations, respectively. The subscript differentiates the edge component from the screw component.

By proposing the solution in the form of trial functions as suggested in Eq. (2) and applying the variational principle, we transform the integral-differential Eq. (1) into an optimization problem. The left part of Eq. (1) is transformed into the elastic energy $E_{\rm el}$ [13],

$$\begin{aligned} E_{\rm el} = {} & H_{11}\left[\sum_{i,j} p_i p_j \ln\left(\frac{R}{w_i+w_j}\right) - \sum_{i<j} p_i p_j \ln\left(1+\frac{r_{e,ij}^2}{(w_i+w_j)^2}\right)\right] \\ & + H_{33}\left[\sum_{i,j} q_i q_j \ln\left(\frac{R}{v_i+v_j}\right) - \sum_{i<j} q_i q_j \ln\left(1+\frac{r_{s,ij}^2}{(v_i+v_j)^2}\right)\right] \\ & + 2H_{13}\left[\sum_{i,j} q_i p_j \ln\left(\frac{R}{v_i+w_j}\right) - \frac{1}{2}\sum_{i,j} q_i p_j \ln\left(1+\frac{r_{ij}^2}{(v_i+w_j)^2}\right)\right]. \end{aligned} \tag{3}$$

The last two terms in Eq. (3) vanish since the dislocation core structure is symmetric. In this expression, H is the Stroh tensor. $\{H_{11}, H_{33}\}=\{K_e, K_s\}$, and $p_1 = p_2 = \frac{b}{2}$, $q_1 = -q_2 = \frac{\sqrt{3}b}{6}$. The terms in the first bracket represent the elastic energy of the edge component, the second stands for the elastic energy of the screw component. The half widths of the partials are $w_1 = w_2 = w_e$, $v_1 = v_2 = w_s$. R is the outer cutoff radius, r_{ij} is the distance between the edge component of Peierls dislocation j and screw component of Peierls dislocation i, and $r_{e,ij}$ or $r_{s,ij}$ is the distance between the edge or screw components of the Peierls dislocations i and j. The distance $r_{e,12} = d_e$ applies for edge components and $r_{s,12} = d_s$ for screw components. The right part is transformed into the misfit energy E_A, i.e., the integral of the gamma surface within the core region of a dislocation:

$$E_A = \int_{-R}^{R} \gamma(u_x(x), u_z(x))dx. \tag{4}$$

In our present work, we take the gradient of the misfit energy E_A as Peierls stress. The solutes are in the current model placed at positions where they have the strongest effect on the gamma surface (see Sec. II B). Since they remain fixed to the positions during the dislocation motion, the current model provides an upper bound for the Peierls stresses at the studied solute concentrations. Since the stress field far away from the dislocation core does not affect the core structure, a large but finite R is sufficient for the evaluation. In the present study, we take $R = 5000b$, where b is the length of the Burgers vector of a basal $\langle a\rangle$ dislocation. A larger R does not change the numerical solutions. The total energy of a dislocation is the sum of the misfit energy and the elastic energy,

$$E_{\rm tot} = E_{\rm el} + E_A. \tag{5}$$

Minimizing the total energy $E_{\rm tot}$ to create a dislocation is equivalent to solving Eq. (1). Therefore we minimize $E_{\rm tot}$ [see Eq. (5)] in our present study in order to determine the geometry (characterized by the parameters w and d) of the studied dislocations. To conduct the minimization, we use the particle swarm algorithm (PSA). This algorithm can effectively avoid local minima in the solution space and identify the optimal solution [22–24].

B. Computational parameters

Our quantum-mechanical calculations of generalized stacking fault energies (GSFEs) were carried out with the Vienna *ab initio* simulation package (VASP) [25] using the projector augmented wave functions and the generalized gradient approximation, with the electron exchange-correlation function described by the Perdew-Burke-Ernzerhof parametrization [26]. A plane-wave cutoff energy of 350 eV is used both for pure Mg and Mg alloys. To sample the Brillouin zone, the Gamma-point-based scheme is employed and the k-point mesh is optimized to guarantee the convergence of the computed total energies. The convergence criterion of the total energy is 10^{-4} eV, i.e., electronic structure iterations stop when the energy difference between two subsequent electronic steps is smaller than this value. The computed lattice constants for pure Mg, $a = 3.189$ Å and $c/a = 1.626$, are in very good agreement with experimental data, $a = 3.206$ Å and $c/a = 1.624$ [21]. For all Mg alloys considered in this study, the lattice parameters were also optimized. We only show the lattice parameters of pure Mg and $Mg_{47}Y$ in Table II.

The generalized stacking fault energy (GSFE) profiles are then computed by changing the out-of-glide-plane primitive vector of the supercell in Cartesian coordinates (see, e.g.,

TABLE II. DFT computed lattice parameters of pure Mg and a $Mg_{47}Y$ alloy.

Stoichiometry	a (Å)	c/a
Mg	3.189	1.626
Mg-Exp. [21]	3.206	1.624
$Mg_{47}Y$	3.206	1.622

Refs. [27,28]). When a fraction of the slip direction vector is consecutively added to the primitive vector until the total vector is reached, the supercell and its image together represent a series of supercells that gradually model the gliding and thus the corresponding GSFEs. Specifically, the gamma surface of the basal plane in pure Mg is first divided into a 20×20 mesh and the total energy is calculated at each grid point. All atoms are relaxed along the direction perpendicular to the simulated glide plane.

More specifically, two perpendicular vectors $\frac{1}{3}[11\bar{2}0]$ and $[10\bar{1}0]$ are selected within the $\{0001\}$ plane and all possible slip displacements can be written as a combination of these two vectors. Suppose u_x/a and $u_z/\sqrt{3}a$ are fractional displacements along these two directions determined by the selected vectors, the GSF vector $\vec{f}$ is then written as

$$\vec{f} = \frac{u_x}{a}\frac{1}{3}[11\bar{2}0] + \frac{u_z}{\sqrt{3}a}[10\bar{1}0], \tag{6}$$

where $0 \leqslant u_x \leqslant a$ and $0 \leqslant u_z \leqslant \sqrt{3}a$. More details about computing gamma surfaces can be found, e.g., in Refs. [27,28].

In order to eliminate any spurious interactions between (i) extended defects (i.e., a glide plane) within the computational supercells and (ii) their periodic images created when applying periodic boundary conditions, the supercell sizes were optimized by performing convergence tests. Specifically, in our supercells, there are two atoms in each direction within the slip plane (four atoms in total in the plane). To test the convergence of our computed generalized stacking fault energies, the number of atoms in the third direction, along the $\langle c \rangle$ direction, which is equivalent to the number of layers within the supercell, was varied (2, 4, 6, 8, and 12 atomic layers). The GSFEs difference between six layers ($2 \times 2 \times 6$, i.e., 24 atoms) and 12 layers ($2 \times 2 \times 12$, i.e., 48 atoms) is less than 1%. Thus supercells with more than six atomic layers are considered to be large enough to provide accurate results. In our study, a 48-atomic supercell (i.e., cells with 12 atomic layers) was employed to describe Mg alloys with one Mg atom being replaced by a solute atom X within the glide plane. Therefore, for $Mg_{47}X$, the atom concentration of X in the supercell is 2.08 at.% and the planar concentration is 25 at.%. Our additional calculations show that GSFEs at points A and B (see Fig. 1) are linearly proportional to the planar concentration of yttrium from 25 at.% down to 11 at.% and further to pure Mg. We assume similar trends also in the case of other solutes. In order to compare quantum-mechanical and atomistic approaches, the gamma surface of pure Mg was also calculated using an embedded atom method (EAM) approach with the potential developed by Sun [29]. Using the same supercells as in the *ab initio* calculations, these simulations were performed employing the LAMMPS [30] code.

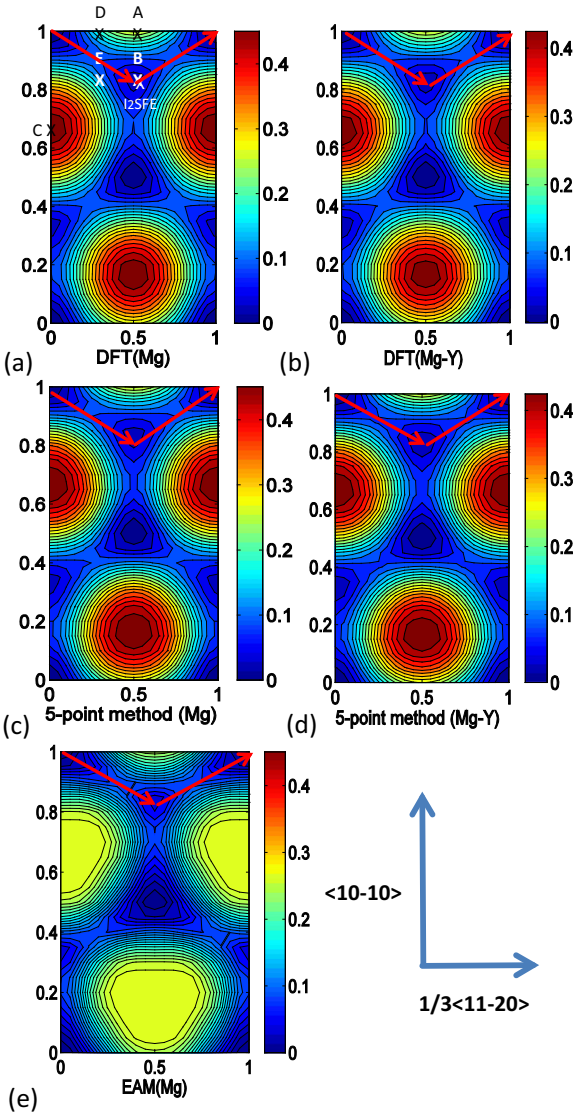

FIG. 1. (Color online) Contour figures of basal-plane gamma surfaces for Mg and Mg-Y alloys computed by DFT [(a) and (b)] and EAM methods (e). The gamma surfaces obtained by applying the five-point approach are shown as well for comparison [(c) and (d)]. The five points A,B,C,D,E that are used as input in our five-point approach are denoted in (a). The minimum energy pathways are indicated by red arrows. The units at the color bars are J m^{-2}.

C. Plane-wave expansion of the gamma surface

Generally, for a crystal, the gamma surface can be expressed by the displacement vector $\vec{u} = (u_x, u_z)$,

$$\gamma(\vec{u}) = \sum_{\vec{G}} c_{\vec{G}} \exp(i\vec{G}\vec{u}), \tag{7}$$

where $\vec{G} = (m\frac{2\pi}{a_x}, n\frac{2\pi}{a_z}), m,n = 0, \pm 1, \pm 2, \ldots, \pm\infty$, a_x and a_z are the lengths of one period of the computational supercell along the x and z directions, so that $\gamma(\vec{u}) = \gamma(\vec{u} + \vec{T})$, translation vector $\vec{T} = (a_x, a_z) = (a, \sqrt{3}a)$. The coefficient $c_{\vec{G}}$ can be calculated by the Fourier transform

$$c_{\vec{G}} = \frac{1}{a_x a_z} \iint_{(0,0)}^{(a_x,a_z)} \gamma(u_x,u_z) \exp(-i\vec{G}\vec{u}) du_x du_z. \tag{8}$$

Writing $c_{\vec{G}} = R_{\vec{G}} + i I_{\vec{G}}$, the gamma surface can be reformulated as

$$\gamma(\vec{u}) = \sum_{\vec{G}} R_{\vec{G}} \cos(2\vec{G}\vec{u}) - I_{\vec{G}} \sin(2\vec{G}\vec{u}), \tag{9}$$

where $\vec{G}$ defines the reciprocal space of the gamma surface. After being Fourier transformed, the gamma surface can be represented by discrete points in reciprocal space. Each of these points corresponds to one coefficient of the terms shown in Eq. (7). Since $\gamma(\vec{u})$ is a real number, the imaginary terms have been excluded in Eq. (9). A more common and computationally more intuitive definition would be to introduce a cutoff wave function, i.e., all

$$|\vec{G}| = \frac{2\pi}{\sqrt{3}a}\sqrt{3m^2+n^2} \leqslant G_k = k\frac{2\pi}{\sqrt{3}a} \tag{10}$$

will be included. In the following, we will use k to denote the plane-wave cutoff, and the corresponding gamma surface is represented by γ_k.

III. FIVE-POINT APPROACH

As stated above, the energetics of the full 2D gamma surface is the key input in Eq. (5). Unfortunately, quantum-mechanical calculations that determine these energies with a high accuracy, are computationally rather costly. As we are aiming at a rapid high-throughput testing of different solutes, lengthy calculations of hundreds of energies within dense meshes covering the gamma surface are not feasible. Therefore, in order to reduce the computational costs, we below propose an approach within which the energies of only five specific points are shown to be sufficient for accurately studying the core structure of $\langle a \rangle$ dislocations in hcp materials. Our approach will be validated for Mg and Mg-Y alloys.

The gamma surface of the basal plane in pure Mg has a threefold symmetry [Fig. 1(a)]. Within the unit cell there are three symmetry equivalent global unstable stacking fault energies (0.473 J m^{-2}) and three symmetry equivalent stable stacking fault energies (0.037 J m^{-2}). The minimum energy path along the $\langle 11\bar{2}0 \rangle$ direction starts from the point corresponding to a perfect crystal and goes through a stable stacking fault energy to later reach another point corresponding to the perfect crystal (see red arrows). For the Mg-Y alloy, the threefold symmetry of the gamma surface [Fig. 1(d)] is slightly broken due to the addition of yttrium lifting the degeneracy of the three global unstable stacking fault energies (0.440, 0.440, and 0.438J m^{-2}).

For comparison, the identical gamma surface is also computed employing the EAM potential [Fig. 1(e)]. The EAM gamma surface shares the same qualitative features as the DFT one, but the maximum GSFE is significantly lower (see the color-coded scale). This difference results in a significantly different barrier along the minimum energy path.

As our aim is to determine the Peierls stress of the basal $\langle a \rangle$-type edge dislocation, we analyze the sensitivity of the derived Peierls stress on the approximation used to fit the gamma surface. For this purpose, we construct a series of gamma surfaces with a different plane-wave cutoff k [in Eq. (10)]. Starting with a high cutoff ($k = 10$), we find that only very few plane-wave coefficients are larger than 10^{-1} mJ m^{-2} (i.e., are smaller than the estimated accuracy of DFT method) indicating that the majority of the terms equals to zero. This indicates that the Fourier representation rapidly converges implying that an accurate representation of the gamma surface can be achieved by only a few low-frequency terms.

TABLE III. Geometrical parameters and Peierls stresses of the $\langle a \rangle$-type basal-plane edge dislocation calculated for different plane-wave cutoffs (denoted by k).

(a) pure Mg

k	d_e/b	d_s/b	w_e/b	w_s/b	τ/MPa
2	8.799	9.087	0.997	0.865	0.026
4	6.970	7.119	0.664	0.574	0.98
5	6.979	7.143	0.668	0.581	1.15
10	7.008	7.183	0.677	0.597	1.15
five-point	6.947	7.097	0.649	0.579	1.08

(b) Mg-Y alloy

k	d_e/b	d_s/b	w_e/b	w_s/b	τ/MPa
2	9.116	9.601	1.064	0.946	0.022
4	8.961	9.172	0.714	0.582	0.55
5	8.964	9.173	0.704	0.570	0.52
10	8.913	9.077	0.704	0.564	0.46
five-point	8.956	9.086	0.698	0.607	0.58

For each of the thus constructed gamma surfaces, we calculated the dislocation core structure parameters (listed in Table III and visualized in Fig. 2). Both the edge and screw components quickly converge for both pure Mg [Figs. 2(a) and 2(b)] and Mg-Y alloys [Figs. 2(c) and 2(d)]. When all plane waves with coefficients smaller than G_4 ($k \leqslant 4$) are included into the gamma surface, the computed dislocation core structures are convergent.

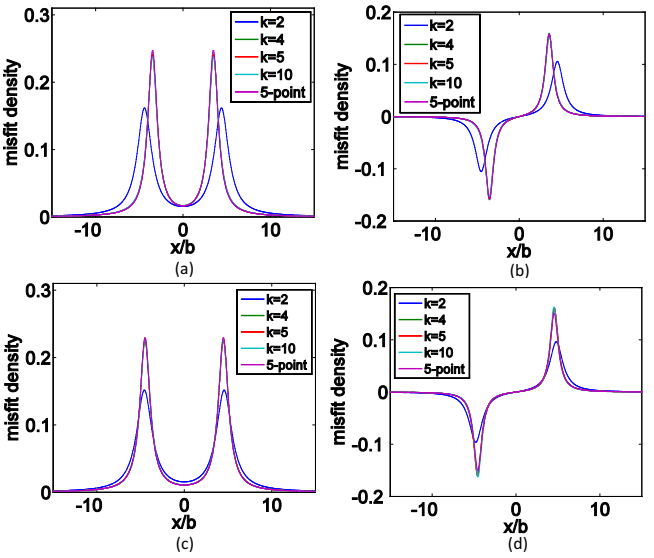

FIG. 2. (Color online) Convergence of the core structure of the $\langle a \rangle$-type edge dislocation with increasing number of plane waves for (a) the edge and (b) the screw components of a dislocation in Mg, and (c) the edge and (d) the screw components of a dislocation in the Mg-Y alloy.

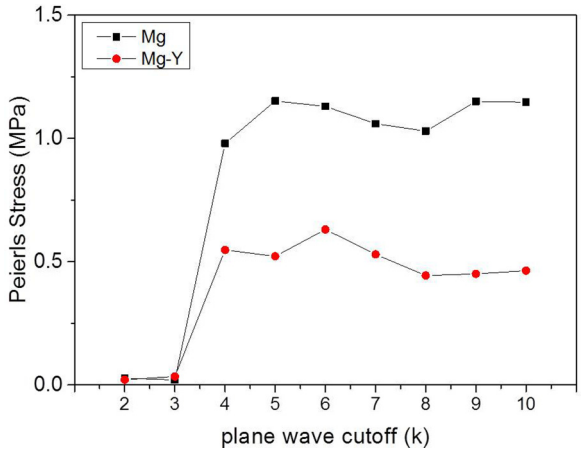

FIG. 3. (Color online) Convergence of the Peierls stress of the ⟨a⟩-type edge dislocation in pure Mg and Mg-Y as a function of the plane-wave cutoff.

Figure 3 shows that the Peierls stress is very sensitive to the number of plane waves used to approximate a gamma surface. The Peierls stress of pure Mg and Mg-Y is almost 0 MPa when $k = 2$ or 3, and then increases to 0.98 MPa (0.55 MPa for Mg-Y) before it becomes converged. Therefore the Peierls stress is a more stringent test than the core structure to identify an accurate plane-wave cutoff. In the following, we choose $k = 5$, which is a good compromise between accuracy and computational efficiency (error in the Peierls stress: $<1\%$ for pure Mg; $<13\%$ for Mg-Y).

The threefold symmetry of the gamma surface of Mg can be used to substantially reduce the number of independent coefficients in the Fourier expansion. We therefore employ the concept of symmetrized plane waves where the simple plane waves are replaced by linear combinations that preserve the desired symmetry. Limiting the plane waves in the range of $k \leqslant 5$, we include the first three symmetrized plane waves (plane waves with coefficients $> 10^{-1}$ mJ m^{-2}) into the analytical expression of the gamma surface [Eq. (11)],

$$\begin{aligned}\gamma_{\text{five-point}}(u_x,u_z) =& R_0 + R_1\left\{\cos\left[2\pi\left(\frac{u_x}{a}-\frac{u_z}{\sqrt{3}a}\right)\right]+\cos\left[2\pi\left(\frac{u_x}{a}+\frac{u_z}{\sqrt{3}a}\right)\right]+\cos\left(4\pi\frac{u_z}{\sqrt{3}a}\right)\right\}\\ &+ R_2\left\{\cos\left[2\pi\left(\frac{u_x}{a}-\frac{3u_z}{\sqrt{3}a}\right)\right]+\cos\left[2\pi\left(\frac{u_x}{a}+\frac{3u_z}{\sqrt{3}a}\right)\right]+\cos\left(4\pi\frac{u_x}{a}\right)\right\}\\ &+ R_3\left\{\cos\left[4\pi\left(\frac{u_x}{a}+\frac{u_z}{\sqrt{3}a}\right)\right]+\cos\left[4\pi\left(\frac{u_x}{a}-\frac{u_z}{\sqrt{3}a}\right)\right]+\cos\left(8\pi\frac{u_z}{\sqrt{3}a}\right)\right\}\\ &+ I_1\left\{\sin\left[2\pi\left(\frac{u_x}{a}-\frac{u_z}{\sqrt{3}a}\right)\right]-\sin\left[2\pi\left(\frac{u_x}{a}+\frac{u_z}{\sqrt{3}a}\right)\right]+\sin\left(4\pi\frac{u_z}{\sqrt{3}a}\right)\right\}\\ &+ I_2\left\{\sin\left[4\pi\left(\frac{u_x}{a}-\frac{u_z}{\sqrt{3}a}\right)\right]-\sin\left[4\pi\left(\frac{u_x}{a}+\frac{u_z}{\sqrt{3}a}\right)\right]+\sin\left(8\pi\frac{u_z}{\sqrt{3}a}\right)\right\}, \qquad (11)\end{aligned}$$

where a is the lattice parameter. In this expression, one group of sin-type functions is dropped since their coefficients are smaller than 10^{-2} mJ m^{-2}.

For convenience, the analytic expression $\gamma_{\text{five-point}}$ [Eq. (11)] is referred as five-point expression. The five coefficients in the equation can be determined by five symmetry inequivalent points on the gamma surface [the sixth coefficient is excluded since its value can be determined by $\gamma_{\text{five-point}}(0,0) = 0$]. The dislocation core structures and Peierls stresses computed by our five-point approach are marked in Table III as "five-point." The results computed by the five-point approach are in good agreement with those computed by the converged gamma surface (γ_{10}, see Sec. II C). The maximum error bar we observe is for the Peierls stress of the Mg-Y alloy (which is the most sensitive quantity) and is about 24%. The sources of these errors are discussed in detail in Appendix.

The gamma surfaces for Mg and Mg-Y approximated by Eq. (11) are shown in Figs. 1(b) and 1(d). They reproduce the key characteristics of the quantum-mechanically calculated ones [Fig. 1(a)]. The predicted stable stacking fault energies and unstable stacking fault energies agree well with the ones derived by DFT simulations. For pure Mg, the predictive quality of our method is much better than that of the computationally inexpensive EAM simulation [Fig. 1(e)], which only qualitatively reproduces the main features.

IV. GENERALIZED STACKING FAULT ENERGIES OF MG ALLOYS

Even though any set of five symmetry inequivalent data points in the basal-plane gamma surface would be sufficient to compute the gamma surface according to Eq. (11), not all possible data points are an equally good choice. On the one hand, data points that are spatially too close may result in noticeable numerical errors. Moreover, the data points around the minimum energy path in the gamma surface are particularly important. We therefore choose the five data points A, B, C, D, and E, marked in Fig. 1(a). The I_2 stacking fault energy (B), the unstable SFE along the ⟨a⟩-type direction (A) and the global maximum USFE (C) have also a clear physical meaning and significance. In pure hcp metals, the I_2 stacking fault energy (B) is usually considered to be the maximum energy barrier that dissociated dislocations of the same type must overcome to move. Thus this quantity is directly related to the mobility of dissociated ⟨a⟩-type dislocations. Similarly, point A is relevant to the mobility of perfect ⟨a⟩-type dislocations. Finally, the point C is the barrier to nucleate the dislocations. In addition to these three points, the two points C and D that are close to the minimum energy path are selected.

To analyze chemical trends in solid solution effects, a set of 20 solutes with either hcp or double hcp crystal structures is

TABLE IV. Generalized stacking fault energies of five selected points (see text) in the basal-plane gamma surface for 20 $Mg_{47}X$ alloys, which are applied in fitting Eq. (11). The planar and bulk concentrations are 25 and 2.08 at.%, respectively.

Solute	A J m^{-2}	B J m^{-2}	C J m^{-2}	D J m^{-2}	E J m^{-2}
Mg	0.275, 0.288 [31]	0.037, 0.036 [31], 0.033 [32],	0.473	0.159	0.158
Mg-Exp.		0.060–0.15 [33]			
Y	0.213, 0.248 [31]	0.010, 0.025 [31]	0.446	0.145	0.146
Be	0.277	0.038	0.476	0.154	0.166
Co	0.302	0.077	0.495	0.168	0.191
Er	0.258	0.027	0.448	0.145	0.152
Hf	0.267	0.036	0.458	0.149	0.160
Ho	0.257	0.025	0.447	0.145	0.151
La	0.234	0.001	0.422	0.132	0.132
Lu	0.262	0.029	0.453	0.152	0.155
Nd	0.242	0.011	0.430	0.137	0.139
Os	0.302	0.083	0.491	0.168	0.193
Pr	0.240	0.008	0.428	0.135	0.137
Re	0.301	0.078	0.491	0.167	0.191
Ru	0.308	0.085	0.502	0.170	0.197
Sc	0.271	0.036	0.465	0.151	0.162
Tc	0.306	0.080	0.498	0.169	0.194
Ti	0.275, 0.355 [31]	0.042, 0.036 [31]	0.469	0.153	0.166
Tl	0.282	0.035	0.485	0.158	0.168
Tm	0.260	0.028	0.451	0.146	0.154
Zn	0.279, 0.256 [31]	0.035, 0.037 [31]	0.480	0.155	0.166
Zr	0.267, 0.328 [31]	0.038, 0.026 [31]	0.457	0.149	0.160

selected from the periodic table of the elements. The five data points (GSFEs) computed by DFT for these 20 Mg alloys are listed in Table IV and visualized in Fig. 4. According to the values of the GSFEs, the following five sequences are obtained (pure Mg and Mg-Y are marked in bold):

According to A: **Y**<La<Pr<Nd<Ho<Er<Tm<Lu<Zr <Hf<Sc<Ti<**Mg**<Be<Zn<Tl<Re<Os<Co<Tc<Ru;

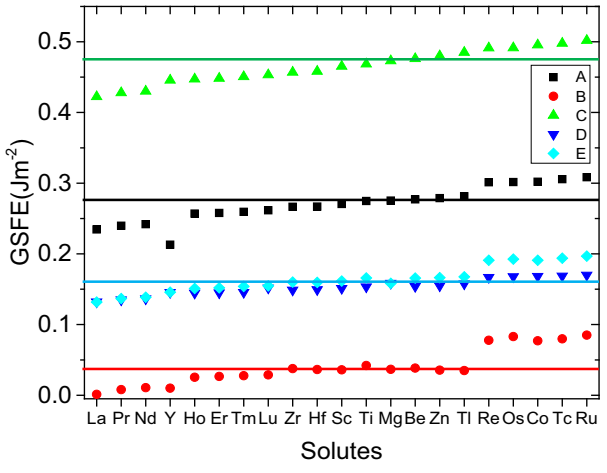

FIG. 4. (Color online) The five GSFEs for 20 Mg alloys (the planar and bulk concentrations are 25 and 2.08 at.%, respectively). The positions of these GSFEs in the 2D gamma surface are marked in Fig. 1(a). Full horizontal color lines denote the GSFEs of pure Mg.

According to B: La<Pr<**Y**<Nd<Ho<Er<Tm<Lu<Tl <Zn<Sc<Hf<**Mg**<Zr<Be<Ti<Co<Re<Tc<Os<Ru;

According to C: La<Pr<Nd<**Y**<Ho<Er<Tm<Lu<Zr <Hf<Sc<Ti<**Mg**<Be<Zn<Tl<Re<Os<Co<Tc<Ru;

According to D: La<Pr<Nd<Ho<Er<**Y**<Tm<Zr<Hf <Sc<Lu<Ti<Be<Zn<Tl<**Mg**<Re<Os<Co<Tc<Ru;

According to E: La<Pr<Nd<**Y**<Ho<Er<Tm<Lu<**Mg** <Hf<Zr<Sc<Be<Ti<Zn<Tl<Co<Re<Os<Tc<Ru.

Any two of these five sequences are different from each other. However, the sequences for A and C are almost same except that the positions of yttrium are different. These trends can be more clearly observed in Fig. 4. The different sequences indicate that the alloying elements do not change the gamma surface in a simple manner, i.e., one that can be described by a single scaling factor. Therefore care should be taken when extending the analysis of gamma surfaces to different concentrations of solutes. However, some general trends may be deduced. For example, if the unstable GSFEs (e.g., A or C) are lower, the corresponding I_2SFEs (B) are lower, too.

The rare-earth elements (RE) reduce all five GSFEs of pure Mg (except Sc in sequence E). However, the non-rare-earth elements (non-RE) generally increase the GSFEs but with some exceptions, e.g., Zr and Hf in sequence A. The maximum values of all five parameters are those computed for the Mg-Ru system, and the minimum ones are those of Mg-La. Ruthenium increases the GSFEs ($A - E$) of pure Mg by 0.01–0.05 J m^{-2}. La can reduce the GSFEs ($A - E$) of pure Mg by 0.02–0.04 J m^{-2}. Interestingly, the I_2SFE (B) of Mg-La is 1 mJ m^{-2}, very close to 0, followed by Mg-Pr, 8 mJ m^{-2}, and Mg-Nd, 11 mJ m^{-2}. The other elements change the GSFEs moderately. Next to our values, Table IV also lists published theoretical and experimental GSFEs. For Mg, the published theoretical data validate our GSFEs of points A and B. Comparing the GSFEs with the experimental data [33] shows that the lower experimental bound is a factor of two larger than the theoretical value. The reason may be that the stacking fault energy in pure Mg is rather small, making an accurate experimental determination of this value challenging. The I_2SFEs of Mg-Y, Mg-Ti, Mg-Zn, and Mg-Zr published by Muzyk *et al.* [31] agree well with the ones presented here. The USFE (at point A) of Mg-Y is also very close to our result, while those of Mg-Zn, Mg-Ti, and Mg-Zr are slightly different. These differences might arise from the different computational methods and slightly different VASP input parameters.

V. DISLOCATION PROPERTIES

A. Pure Mg

The gamma surface of pure Mg was evaluated by both EAM (employing the Finnis-Sinclair potential developed by Sun [29]) and DFT for comparison. Since the gamma surface shapes obtained by EAM and DFT are quite different, the dislocation cores obtained using the PN method are also very different. The predicted stacking fault width (distance between the two dissociated partial dislocations) by the PN model using the EAM gamma surface is $\approx 3b$, and the one obtained by DFT $\approx 7b$. Hence the EAM predicted dislocation core is much more compact than the one derived by DFT. The difference can be explained by the theory of the Volterra dislocations. The

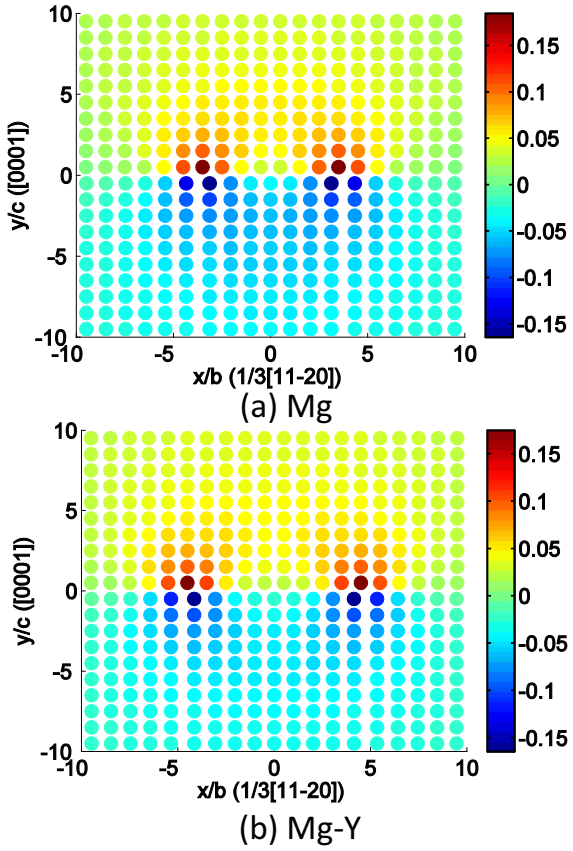

FIG. 5. (Color online) The core structures of pure Mg and the Mg-Y alloy. The color bar denotes the hydrostatic stress in GPa. The colored atoms clearly show the location of two partial dislocations with a stacking fault in between, b and c are the lengths of one period in each direction.

stacking fault width of a Volterra dislocation (here basal $\langle a \rangle$ dislocation) is inversely proportional to the I_2 stacking fault energy. Indeed, EAM predicts a higher I_2 stable stacking fault energy (48 mJ m^{-2}) than DFT (I_2SFE = 37 mJ m^{-2}).

To conveniently compare the dislocation core computed by atomistic simulations, the dislocation core of Mg by our method is visualized in Fig. 5(a). Here, the parameters of the core structure are employed to compute the hydrostatic stress field around the dislocation [24] in Mg, which is used as a parameter to color the atoms. The colored atoms clearly indicate the location of the two partial dislocations that are separated by the I_2 stacking fault.

Wang *et al.* employed a modified Peierls-Nabarro model (including a new gradient term, which is considered to be important to describe dislocations having a narrow core) to calculate the dislocation core structure of pure Mg [34]. The stacking fault width calculated in Wang's work is 6.7b and in excellent agreement with ours, 7b. Applying the modified model with the gradient terms they predicted a much wider half width (e.g., w_d,w_s) for each partial. The planar core was computed directly by Yasi *et al.* [6] using both DFT and a Finnis-Sinclair EAM potential [29]. The predicted stacking fault widths were 5.2b (DFT) and 4.5b (EAM), respectively. The fully atomistic dislocation core predicted by DFT is slightly smaller than the one predicted here by DFT using Peierls-Nabarro model, but their fully atomistic EAM dislocation core is slightly wider than our Peierls-Nabarro one using the same EAM potential. Shin and Carter [7] computed the same stacking fault width using obital-free DFT, i.e., 7.6–8.0 b, which is very close to our result.

The Peierls stress computed by our approach and using the DFT derived gamma surface is 1.08 MPa at 0 K, about 1/20 (i.e., more than one order of magnitude) of that using the EAM gamma surface (22.9 MPa at 0 K). The DFT value is significantly closer to the experimental values observed in pure Mg single crystals (0.5–0.8 MPa) although it is still a factor of two too high. Using the fully DFT computed gamma surface [i.e., without using the approximate five-point formula Eq. (11)], we find a slightly larger value for the Peierls stress of 1.15 MPa at 0 K, i.e., the deviation from the experiment is not related to this approximative description of the gamma surface.

TABLE V. Geometrical parameters of dislocation cores and Peierls stresses for 20 solute solution Mg alloys computed by the five-point approach.

Solute	d_e/b	d_s/b	w_e/b	w_s/b	τ_p/MPa
Mg-DFT1[a]	7.00	7.18	0.68	0.60	1.15
Mg-DFT2[b]	6.95	7.10	0.65	0.59	1.15
	6.7 [34]	6.7 [34]	3.7 [34]	3.0 [34]	
Mg-Exp.[c]					0.52–0.81[35–37]
Mg-EAM1[d]	3.06	2.90	0.45	0.38	22.9
Mg-EAM2[e]	4.48 [6]				
Mg-FBC[f]	5.2 [6]				
Mg-OFDFT[g]	7.6–8.0 [7]				
Y	8.91	9.08	0.70	0.56	0.46
Be	6.98	7.07	0.61	0.52	1.90
Co	3.03	3.16	0.55	0.48	6.60
Er	12.93	13.00	0.67	0.56	0.59
Hf	6.99	7.09	0.64	0.54	1.57
Ho	10.96	11.04	0.66	0.56	0.83
La	19.18	19.24	0.72	0.59	1.65
Lu	8.96	9.06	0.64	0.55	1.30
Nd	13.10	13.18	0.69	0.58	1.18
Os	3.01	3.15	0.56	0.49	5.41
Pr	17.09	17.15	0.69	0.58	1.70
Re	3.03	3.17	0.56	0.48	6.02
Ru	3.01	3.14	0.55	0.48	5.59
Sc	8.93	9.01	0.63	0.53	0.88
Tc	4.82	4.92	0.58	0.51	4.30
Ti	6.95	7.05	0.62	0.53	1.17
Tl	7.00	7.10	0.59	0.50	2.96
Tm	10.94	11.00	0.65	0.54	0.70
Zn	6.94	7.11	0.64	0.52	2.53
Zr	6.98	7.09	0.64	0.54	1.47

[a]The gamma surface γ_{10} by DFT.
[b]The gamma surface $\gamma_{\text{five-point}}$ by DFT.
[c]Experimental results.
[d]The gamma surface computed by the Finnis-Sinclair-EAM potential.
[e]Direct simulation of dislocation using the Finnis-Sinclair-EAM potential.
[f]Flexible boundary condition using DFT.
[g]Orbital-free DFT.

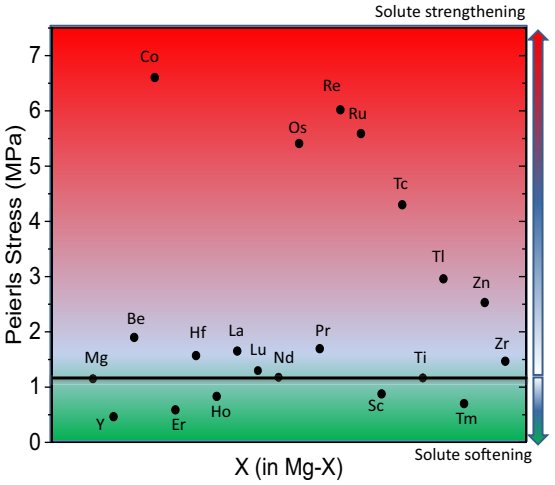

FIG. 6. (Color online) Peierls stresses of 20 different Mg solute solution alloys predicted by using the Peierls-Nabarro model in conjuction with the five-point approach, Eq. (11). The black line corresponds to the Peierls stress of Mg as a reference.

B. Mg alloys

Employing our five-point approach, the dislocation core structures and Peierls stresses of 20 different solid solution Mg alloys are computed and their characteristics are summarized in Table V. As an example, the dislocation core structure of Mg-Y is shown in Fig. 5(b). The Peierls stress caused by the various solutes is visualized in Fig. 6. The black line in Fig. 6 denotes the Peierls stress of pure Mg as a reference measure. Solutes that lie in their respective effects above the Mg reference line increase the Peierls stress of Mg, i.e., they lead to a solute strengthening effect; solutes below the line reduce the Peierls stress, i.e., they cause solute softening.

However, when the error bar of the Peierls stress is considered (see Appendix for detail), the impact of the solute on the Peierls stress cannot be predicted if the change is small. Therefore the solutes are divided into three groups: (i) solutes pertaining to the first group, including Be, Zn, Tl, Tc, Os, Ru, Re, and Co lead to more compact dislocation core structures (3.0 b to 7.1 b, $b = 3.19$ Å) and larger Peierls stresses than pure Mg (1.9 to 6.6 MPa) when added as solutes into Mg. (ii) Elements in the second group, including Ti, Nd, Lu, Zr, Hf, La, and Pr change the stacking fault widths from 7.0 b to 19.2 b and Peierls stresses moderately (1.2 to 1.7 MPa). (iii) Solute elements in the third group include Y, Er, Tm, Ho, and Sc extend the core width from 8.9 b to 12.9 b, and the resulting Peierls stresses are generally very low (0.46 to 0.88 MPa). Assuming that the error bar of the Mg-Y alloy is representative to all Mg alloys, we conclude that the first group is able to strengthen the basal $\langle a \rangle$ dislocation, while the third group softens them. The effect of the second group is, however, quite small to render distinct alloy design rules from this effect.

VI. CONCLUSIONS

The gamma surfaces of Mg and 20 different solid solution Mg alloys have been systematically studied employing both quantum-mechanical and atomistic simulations and used as input to determine the dislocation core structures and Peierls stresses of basal-plane ⟨a⟩-type edge dislocations within a Peierls Nabarro model. We summarize our most important conclusions as follows.

(i) The gamma surface of basal-plane ⟨a⟩-type edge dislocations in hcp materials can be well approximated by a Fourier series with only a few terms. Specifically, coefficients determined from the knowledge of only five special points within the generalized stacking fault energy surface are found to be sufficient. The computational efficiency of this approach allows us to systematically evaluate the influence of a large number of solute atoms in Mg and to derive chemical trends.

(ii) Within the framework of our approach, dislocation cores and Peierls stresses of pure Mg, computed by using EAM and DFT derived gamma surfaces are compared. This comparison shows that the present parameterization of the Mg potential is not sufficient and gives rise to large errors in the computed Peierls stress. This argument of having not sufficiently accurate parameter sets is even more critical for Mg alloys. Therefore the proposed approach provides a computationally efficient and sufficiently reliable method to study the influence of solutes on the dislocation core geometry and some of the associated solid solution effects.

(iii) Our analysis of 20 different solutes shows that the energetics of the gamma surfaces cannot be described by a simple scaling factor.

(iv) For pure Mg, the predicted basal-plane ⟨a⟩-type dislocation core structure calculated using a DFT derived gamma surface is 7b wide. The calculated Peierls stress is 1.15 MPa at 0 K and close to the reported experimental values.

(v) Among the 20 solutes, Be, Zn, Tl, Tc, Os, Ru, Re, and Co are able to strengthen the basal $\langle a \rangle$ dislocation motion, while Y, Er, Tm, Ho, and Sc soften it. The effects of the other solutes are much less pronounced.

The success of the five-point approach for calculating basal $\langle a \rangle$-type edge dislocations encourages us to continue to use it for prismatic $\langle a \rangle$-type dislocations in a next step. The knowledge about these dislocations will help to improve our understanding on the mechanical behavior of Mg alloys and thus paving the path towards new ductile Mg alloys.

ACKNOWLEDGMENTS

The authors thank G. Leyson for fruitful discussions. Z.P. acknowledges a financial support from the Deutsche Forschungsgemeinschaft (DFG) through a doctoral program of Aachen Institute of Advanced Computational Engineering Science (AICES). M.F. acknowledges financial support from the Academy of Sciences of the Czech Republic through the Fellowship of Jan Evangelista Purkyně and access to the computational resources provided by the MetaCentrum under the program LM2010005 and the CERIT-SC under the program Centre CERIT Scientific Cloud, part of the Operational Program Research and Development for Innovations, Reg. No. CZ.1.05/3.2.00/08.0144.

APPENDIX: SENSITIVITY ANALYSIS

We now analyze how errors in the input parameters of the PN model propagate and affect the final results. We focus here

TABLE VI. Sensitivity analysis of approximations to the gamma surfaces for pure Mg and the Mg-Y alloy in the Peierls-Nabarro model.

(a) Core structure parameters and Peierls stresses computed by the various approximations to the gamma surface.

	γ	d_e/b	d_s/b	w_e/b	w_s/b	τ/MPa
Mg	γ_{10}	7.008	7.183	0.677	0.597	1.15
	γ_5	7.009	7.040	0.668	0.581	1.15
	$\gamma_{\text{five-point}}$	6.947	7.097	0.649	0.579	1.08
Mg-Y	γ_{10}	8.913	9.077	0.704	0.564	0.46
	γ_5	8.964	9.173	0.704	0.570	0.52
	$\gamma_{\text{five-point}}$	8.956	9.086	0.698	0.607	0.58

(b) Error bars of the quantities listed in (a).

	Errors	$d_e/\%$	$d_s/\%$	$w_e/\%$	$w_s/\%$	$\tau/\%$
Mg	E0	0.00	0.00	0.00	0.00	0.00
	E1	0.01	−1.99	−1.33	−2.68	0.44
	E2	−0.88	0.81	−2.84	−0.34	−6.25
	E3	−0.87	−1.20	−4.14	−3.02	−5.84
Mg-Y	E0	0.00	0.00	0.00	0.00	0.00
	E1	0.58	1.05	−0.08	1.09	12.50
	E2	−0.10	−0.95	−0.86	6.38	10.54
	E3	0.48	0.09	−0.94	7.54	24.35

on two test cases: pure Mg and Mg-Y. Apart from systematic errors due to approximating the atomistic system by an approximate PN model, there are three sources of errors entering the Peierls-Nabarro model: (i) the approximation of the elastic energy E_{el} [Eq. (3)]; (ii) the numerical algorithm applied to solve the model; and (iii) the accuracy of representing the gamma surface.

To estimate (i), we notice that the basal plane of an hcp metal can be treated as elastically isotropic. We can therefore ignore the interaction between screw and edge components when expressing the elastic energy. The corresponding error is thus considered to be negligible. To address (ii), we notice that the applied numerical algorithm in this study is a particle swarm optimization. This algorithm is believed to effectively avoid trapping in local minima, nevertheless, this cannot be guaranteed. In order to find the global minimum and avoid local minima, we therefore run the optimization calculations several times with random initial parameters until no further changes in the absolute minimum are observed. Therefore, also this error contribution is well under control. Thus the remaining and major source of errors lies in the representation of the gamma surface.

In order to analyze the propagation of these errors, the results computed by the gamma surfaces (γ_{10}, see Sec. II C) of both Mg and Mg-Y are used below as references. These references are assumed by definition to be error free [see "E0" in Table VI(b)]. By representing the gamma surface of γ_5 and dropping the terms with higher frequencies, we introduce the first error "E1" [see Table VI(b)]. The core structure and the Peierls stresses calculated by the five-point approach includes the approximations of (i) dropping the terms included in γ_5 but excluded from the gamma surface of the five-point approach $\gamma_{\text{five-point}}$ [Eq. (11)] and (ii) using only five points to fit $\gamma_{\text{five-point}}$. These two error sources are merged into the error "E2." For the Mg-Y alloy, the error "E2" also includes the influence of yttrium on the gamma surface symmetry. Total errors introduced by the five-point approach (i.e., with respect to the converged γ_{10} surface) are marked as "E3" in Table VI(b). Applying the data under the lists of γ_{10}, γ_5, and $\gamma_{\text{five-point}}$, these errors can be calculated by the following equations:

$$\begin{aligned} \text{E1} &= \frac{D_{\gamma_5} - D_{\gamma_{10}}}{D_{\gamma_{10}}} \times 100\%, \\ \text{E2} &= \frac{D_{\gamma_{\text{five-point}}} - D_{\gamma_5}}{D_{\gamma_5}} \times 100\%, \\ \text{E3} &= \frac{D_{\gamma_{\text{five-point}}} - D_{\gamma_{10}}}{D_{\gamma_{10}}} \times 100\%, \end{aligned} \tag{A1}$$

where $D_i (i = \gamma_5, \gamma_{10}, \gamma_{\text{five-point}})$ represents the results for the geometric parameters and the Peierls stresses listed in Table VI(a).

Table VI(b) shows the results of these errors. The error bars of our five-point approach are listed as "E3." Generally, the error bars of the Peierls stresses are much larger than those of the core structure parameters. For example, the maximal error bars of the core structure parameters are 4% in pure Mg and 7% in Mg-Y alloy, while for Peierls stresses the error bars can be as large as 6% for pure Mg and 24% for the Mg-Y alloy. Therefore Peierls stresses are more sensitive to approximations to the gamma surfaces than the geometrical parameters describing the core structures: small variations in the core structures are magnified when passing to Peierls stresses. Since adding yttrium atoms slightly breaks the symmetry of the gamma surface, which introduces an additional approximation to the case of Mg, the error bars of Mg-Y are generally larger than those of Mg both in terms of the core structure and the Peierls stress. Since symmetry breaking is expected for all solutes, we assume that the error bars for the alloys are similar as for the Mg-Y.

The errors listed under "E1" (dropping high frequency components in the gamma surface) are less than 3% for pure Mg, which means the smaller terms of the high frequencies (coefficients $<10^{-1}$ mJ m^{-2}) are not important for the case of pure Mg. However, neglecting these terms causes a moderate error for the Mg-Y alloy of 12.5%. Using the five-point formula (11) instead of expressing the gamma surface up to $k = 5$ (i.e., γ_5) introduces errors of about 6% to the value of the Peierls stress and less than 3% to the core structure. In the case of the Mg-Y alloy, this approximation leads to errors of 10.5% for the Peierls stress and up to 6% for the core structure. These error bars validate our approximations and choice of convergence parameters.

[1] K. U. Kainer, *Magnesium Alloys and Technology* (Wiley, New York, 2004).

[2] H. Friedrich *et al.*, *Magnesium Technology* (Springer, Berlin, 2006).

[3] F. Roters, P. Eisenlohr, L. Hantcherli, D. D. Tjahjanto, T. R. Bieler, and D. Raabe, Acta Mater. **58**, 1152 (2010).
[4] D. Raabe, P. Klose, B. Engl, K. P. Imlau, F. Friedel, and F. Roters, Adv. Eng. Mater. **4**, 169 (2002).
[5] T. Nogaret, W. Curtin, J. Yasi, L. G. H., Jr., and D. Trinkle, Acta Mater. **58**, 4332 (2010).
[6] J. A. Yasi, T. Nogaret, D. R. Trinkle, Y. Qi, L. G. H., Jr., and W. A. Curtin, Modell. Simul. Mater. Sci. Eng. **17**, 055012 (2009).
[7] I. Shin and E. Carter, Modell. Simul. Mater. Sci. Eng. **20**, 015006 (2012).
[8] I. Shin and E. A. Carter, Int. J. Plast. **60**, 58 (2014).
[9] J. A. Yasi, L. G. H., Jr., and D. R. Trinkle, Acta Mater. **58**, 5704 (2010).
[10] J. A. Yasi, L. G. H., Jr., and D. R. Trinkle, Acta Mater. **60**, 2350 (2012).
[11] G. Leyson, L. H., Jr., and W. Curtin, Acta Mater. **60**, 5197 (2012).
[12] C. Woodward and S. I. Rao, Phys. Rev. Lett. **88**, 216402 (2002).
[13] G. Schoeck, Mater. Sci. Eng.: A **400-401**, 7 (2005).
[14] G. Leibfried and H. Dietze, Z. Physik **131**, 113 (1951).
[15] V. Vítek, Phil. Mag. **154**, 773 (1968).
[16] S. F. Wang, J. Phys. A **42**, 025208 (2009).
[17] V. V. Bulatov and E. Kaxiras, Phys. Rev. Lett. **78**, 4221 (1997).
[18] G. Lu, N. Kioussis, V. V. Bulatov, and E. Kaxiras, Mater. Sci. Eng. A **309-310**, 142 (2001).
[19] T. Tsuru, Y. Udagawa, M. Yamaguchi, M. Itakura, H. Kaburaki, and Y. Kaji, J. Phys.: Condens. Matter **25**, 022202 (2013).
[20] P. Hirth and J. Lothe, *Theory of Dislocations*, 2nd ed. (Wiley, New York, 1982).
[21] D. Lide, *Handbook of Chemistry and Physics*, 86th ed. (CRC Press, 2005–2006).
[22] J. Kennedy and R. Eberhart, in *Proceedings of IEEE International Conference on Neural Networks, Perth, WA*, Vol. 4 (IEEE, Piscataway, NJ, 1995), p. 1942.
[23] R. Poli, J. Artif. Evol. Appl. **2008**, 1 (2008).
[24] D. Ma, M. Friák, J. von Pezold, D. Raabe, and J. Neugebauer, Acta Mater. **85**, 53 (2015).
[25] G. Kresse and J. Furthmüller, Phys. Rev. B **54**, 11169 (1996).
[26] J. P. Perdew, K. Burke, and M. Ernzerhof, Phys. Rev. Lett. **77**, 3865 (1996).
[27] Z. Pei, L.-F. Zhu, M. Friák, S. Sandlöbes, J. v. Pezold, H. Sheng, C. Race, S. Zaefferer, B. Svendsen, D. Raabe, and J. Neugebauer, New J. Phys. **15**, 043020 (2013).
[28] J. R. Morris, J. Scharff, K. M. Ho, D. E. Turner, Y. Y. Ye, and M. H. Yoo, Phil. Mag. A **76**, 1065 (1997).
[29] D. Y. Sun, M. I. Mendelev, C. A. Becker, K. Kudin, T. Haxhimali, M. Asta, J. J. Hoyt, A. Karma, and D. J. Srolovitz, Phys. Rev. B **73**, 024116 (2006).
[30] S. Plimpton, J.Comp. Phys. **117**, 1 (1995).
[31] M. Muzyk, Z. Pakiela, and K. Kurzydlowski, Scripta Materialia **66**, 219 (2012).
[32] J. Han, X. Su, Z.-H. Jin, and Y. Zhu, Scripta Materialia **64**, 693 (2011).
[33] R. E. Smallmann and P. S. Dobson, Metal. Trans. **1**, 2383 (1970).
[34] R. Wang, S. F. Wang, X. Z. Wu, and Q. Y. Wei, Physica Scripta **81**, 065601 (2010).
[35] E. Schmid, Z. Elektrochem **37**, 447 (1931).
[36] P. W. Bakarian and C. H. Mathewson, Trans. AIME **152**, 226 (1943).
[37] H. Conrad and W. D. Robertson, Trans. AMIE **209**, 503 (1957).